THE ASTROPHYSICAL JOURNAL, 850:130 (8pp), 2017 December 1 https://doi.org/10.3847/1538-4357/aa94ca

3D Polarized Imaging of Coronal Mass Ejections: Chirality of a CME

C. E. DeForest[1], C. A. de Koning[2], and H. A. Elliott[1]
[1] Southwest Research Institute, 1050 Walnut Street Suite 300, Boulder, CO 80302, USA
[2] Cooperative Institute for Research in Environmental Sciences (University of Colorado at Boulder), USA
Received 2017 September 15; revised 2017 October 17; accepted 2017 October 17; published 2017 November 27

Abstract

We report on a direct polarimetric determination of the chirality of a coronal mass ejection (CME), using the physics of Thomson scattering applied to synoptic polarized images from the *Solar Terrestrial Relations Observatories*/COR2 coronagraph. We confirmed the determination using in situ magnetic field measurements of the same CME with the *ACE* spacecraft. CME chirality is related to the helicity ejected from the solar corona along with the mass and field entrained in the CME. It is also important to prediction of the space-weather-relevant *Z* component of the CME magnetic field. Hence, remote measurement of CME chirality is an important step toward both understanding CME physics and predicting geoeffectiveness of individual CMEs. The polarimetric properties of Thomson scattering are well known and can, in principle, be used to measure the 3D structure of imaged objects in the solar corona and inner heliosphere. However, reduction of that principle to practice has been limited by the twin difficulties of background subtraction and the signal-to-noise ratio in coronagraph data. Useful measurements of the 3D structure require relative photometry at a few percent precision level in each linear polarization component of the K corona. This corresponds to a relative photometric precision of order 10^{-4} in direct images of the sky before subtraction of the F corona and related signal. Our measurement was enabled by recent developments in signal processing, which enable a better separation of the photometric signal from noise in the synoptic COR2 data. We discuss the relevance of this demonstration measurement to future instrument requirements, and to the future measurements of 3D structures in CMEs and other solar wind features.

Key words: methods: data analysis – polarization – Sun: coronal mass ejections (CMEs) – techniques: image processing – techniques: polarimetric

1. Introduction

The first image of a coronal mass ejection (CME) was taken on 1971 December 14 (Tousey 1973) by the white-light coronagraph on OSO-7. Today, more than 45 years later, the most common images of CMEs are still single-view, total-brightness, white-light images formed from sunlight that is Thomson-scattered by free electrons in the solar corona. These images do not contain any information about the three-dimensional (3D) structure of plasma and embedded magnetic field that comprises the CME; rather, they project the entire structure onto a 2D focal plane.

Although CMEs are flattened in total-brightness images, the polarization properties of Thomson scattering yield information about the 3D location of dense features. The theory of this process has been developed by many authors (e.g., Billings 1966; Howard & Tappin 2009; DeForest et al. 2013). One of the earliest attempts to use polarized white-light images to analyze internal structure of a CME was by Crifo et al. (1983). They used the fractional polarization of a particular CME to indicate the distance from the sky plane of a cleanly presented, circular-appearing CME. They concluded that the CME was a 3D bubble-like structure, rather than planar loop-like structure.

More recently, several researchers have used polarimetric imaging to analyze the large-scale structure and direction of CMEs. In particular, Moran & Davila (2004) used polarimetric imaging to reconstruct the halo CMEs of 1998 October 31 and 1999 June 29 and concluded that these events were expanding arcade loops. Similarly, Dere et al. (2005) used polarimetric imaging to reconstruct the CMEs of 2002 August 1 and 2002 August 7; they concluded that the August 1 event was an expanding loop arcade, whereas the August 7 event was reminiscent of a flux rope. As Dere et al. (2005) conclude, it is clear that polarization measurements can, at least in principle, play a significant role in understanding CME structure and kinematics.

Despite these promising demonstrations, coronagraph polarization data continue to be under-utilized—even after the 2006 October launch of the twin *Solar Terrestrial Relations Observatory* (*STEREO*; Kaiser et al. 2008) spacecraft, which regularly record sequences of polarized coronal images. In the *STEREO* era, some researchers have used polarimetric imaging to reconstruct CMEs as global structures (Mierla et al. 2010; de Koning & Pizzo 2011; Dai et al. 2015). Others have used COR1 images (Moran et al. 2010) and COR2 images (de Koning 2014) to reconstruct some features that are internal to the CME. In all cases, such reconstructions to date have been limited by low signal-to-noise ratio (S/N). In particular, no 3D analyses of small features have been convincingly demonstrated to be above the noise floor.

The limitation of existing 3D location measurement is that interpreting the polarization signal requires approximately an order of magnitude better S/N than does the direct determination of focal-plane structure. Heavy blurring of the original data (via median-filtering or direct convolution with a blurring kernel) have been required in all published cases to beat down photon noise in the coronagraph signal. This blurring has a limited effect on the noise and incurs the penalty of obscuring the detailed structure of the target CME.

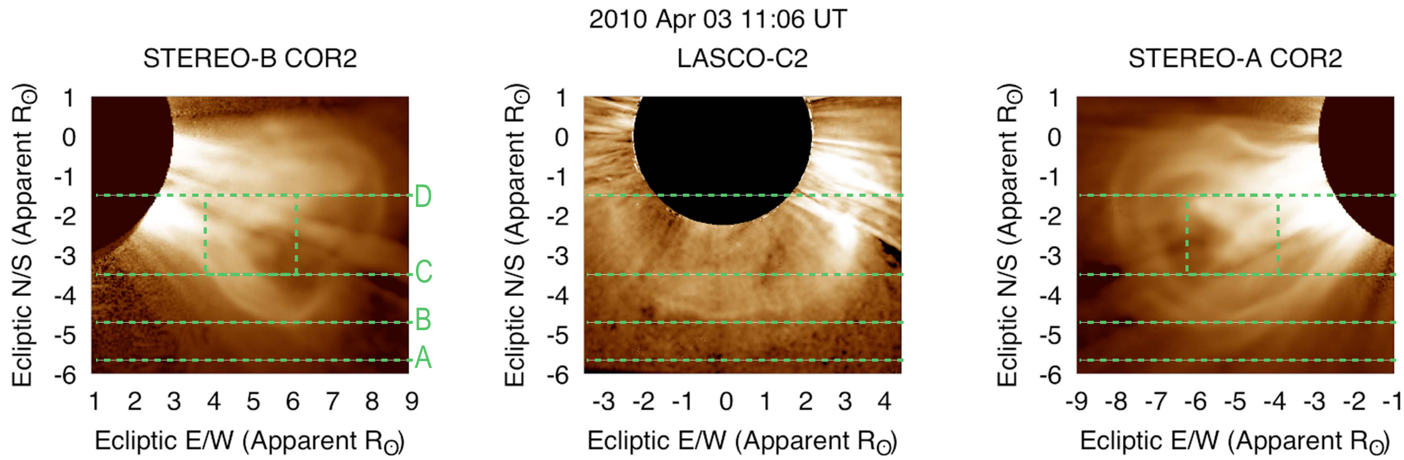

Figure 1. Three views, in visible unpolarized light, of the CME of 2010 April 3 11:08 UT show good correspondence of features across three instruments. At that time, *STEREO-A* was 72° ahead and *STEREO-B* was 67° behind Earth. The views have been calibrated to the same apparent scale and rotated to ecliptic viewing coordinates, so that each plasma structure has approximately the same vertical placement in each image. Several structures are marked here and described in the text. The *STEREO*/COR2 images were processed, as described in the text.

In this paper, we apply a recently developed image noise-reduction technique, *3D noise-gating* (DeForest 2017), to polarized white-light measurements made by *STEREO-A*/COR2 during the CME of 2010 April 3. Noise-gating greatly improves the S/N of the images, allowing us to determine directly the structure of small internal features of the CME, including the location and chirality of the central flux rope. Chirality, in particular, is important because it is closely related to the out-of-ecliptic component of the magnetic field (B_z) of the leading portion of the flux rope as it sweeps across the solar system. This leading B_z is a major predictor of geoeffectiveness in Earth-directed CMEs. Measuring chirality of individual CME structures has not been possible with prior analyses, primarily because measuring the 3D shape of CME substructure requires better photometry than has been available at small image scales.

In Section 2, we describe the observations and the noise-gating process, which improves the image S/N. In Section 3, we recap the processing steps to extract the polarized brightness (*pB*) and total brightness (*B*) from polarized triplets of COR2 images. We also briefly outline how to determine 3D location from these images. In Section 4, we reveal the extracted structures in the CME; in Section 5, we compare them to in situ traces taken through the same structure by the *ACE* spacecraft; and in Section 6, we draw conclusions about this initial measurement and discuss their broader implications for heliophysics, for future measurements, and for requirements on future instruments.

2. Data

We analyzed Thomson-scattered images of the mid corona, collected with the COR2 instrument (Howard et al. 2008) on the *STEREO-A* spacecraft on 2010 April 3. At that time, the COR2 synoptic sequence collected and downlinked a triplet of linearly polarized images of the corona once per hour. The CME was visible in the triplets from (UTC) 10:08, 11:08, and 12:08. For context, we also used coronal images from the LASCO-C2 camera (Brueckner et al. 1995) on board the *Solar and Heliospheric Observatory* (*SOHO*; Domingo et al. 1995).

Figure 1 shows the CME, as seen with *STEREO-B*/COR2, *Solar and Heliospheric Observatory* (*SOHO*)/Large Angle and Spectrometric Coronagraph Experiment (LASCO)-C2, and *STEREO-A*/COR2. All three cameras lay in the ecliptic plane, so parallax effects between the images are confined to moving features horizontally. This happy geometric circumstance allows ready cross-identification of features seen by all three cameras, and several are marked in Figure 1. These images have been background-subtracted, as described below.

The horizontal lines "A" and "B" mark two portions of the outer envelope of the CME, as seen from all three instruments. The overall morphology reproduces the "bubble" shape described by Crifo et al. (1983). The lines "C" and "D" mark the extent of a central bright structure that is most cleanly seen from *STEREO-A* and that is highlighted with a dashed box in both the *STEREO-A* and *STEREO-B* views. We used polarimetry to characterize not only the outer envelope (the arcs tangent to "A" and "B"), but also this small feature that appears to mark the core of the CME.

Historically, photometric and polarimetric analyses of coronal structure have been limited by photon noise because they require percent-level precision in K-coronal brightnesses—which themselves are percent-level perturbations on the F coronal brightness at moderate apparent solar altitudes of a few solar radii. To reduce the observed noise in the *STEREO* data, we used the new technique of *3D noise-gating* (DeForest 2017). Noise-gating identifies image features that are coherent in space and/or time in an image sequence, and separates them from a parametric photon noise floor, based on the features' amplitude in the Fourier transform of each image neighborhood. The technique is useful because it selectively preserves statistically significant features in the data based on coherence, and therefore preserves image structure more completely than does direct convolution or neighborhood median-filtering.

STEREO/COR2 data are collected as polarization triplets that can be combined on the ground. We separated the triplets into three independent image streams of Level 1 data (2048×2048 pixel images prepared with the *STEREO* team's *SECCHI_PREP* software). We removed bright stars from these images on a per-frame basis using the *spikejones* unsharp-masking spike detector (DeForest 2004), then used 2×2 direct binning to decimate the images to 1024×1024 macropixels. We subjected these images to direct noise-gating with $24 \times 24 \times 12$ macropixel ($48 \times 48 \times 12$ native camera pixel) neighborhoods and a threshold of 4 times the inferred noise floor, as described by DeForest (2017). Despiking, binning, and noise-gating together reduced image noise by a factor of more than 30, while preserving image features on the scale of the observed CME structure.

3. Analysis

Thomson-scattered light is polarized by attenuation in the plane of scatter. Therefore the corona appears polarized perpendicular to the radial direction from the Sun, in the focal plane of the instrument (Lyot 1931). The mechanism is projection of the electric field between the planes perpendicular to the incident and departing rays, which arises from the dipolar radiation pattern around the scattering electron (e.g., Jackson 1962). In the context of solar observing, the theory has been published extensively by several authors (e.g., Billings 1966; Howard & Tappin 2009; DeForest et al. 2013). DeForest et al., in particular, include an inversion for determining the out-of-sky-plane angle, ξ, given the degree of polarization.

The brightness from the corona may be imaged directly as brightnesses B_R and B_T seen through radially or tangentially aligned linear polarizers, respectively, but is more commonly divided into unpolarized B and "excess polarized" pB components, with $B \equiv B_T + B_R$ and $\mathrm{pB} \equiv B_T - B_R$ (i.e., pB is just $\pm Q$ or $\pm U$ along vertical, horizontal, or diagonal lines respectively, where Q and U are the familiar Stokes parameters). The polarization triplets from *STEREO* are collected at polarizer angles of 0°, 120°, and 240° relative to a reference angle of 48.°5 in the image plane.

We carried out the pB analysis using direct triplet inversion to recover pB, via the formula

$$pB = \frac{2}{3}\sum_{n=0}^{2}\{[B - 2B_{120n^\circ}]\cos(2\theta)\}, \tag{1}$$

where B_{120n° is the brightness at one polarizer position; all the brightnesses (pB, B, and B_{120n°) are functions of focal-plane radius b and solar position angle θ; and θ is relative to the polarizer reference angle. This is the inversion used by the *STEREO* team's supplied code in the *Solarsoft* system, and arises directly from the observation that

$$B_\phi = B_R(\cos^2(\theta - \phi)) + B_T(\sin^2(\theta - \phi)), \tag{2}$$

where B_ϕ is the brightness observed through a polarimeter oriented at the angle ϕ, and (as above) θ is a polar coordinate in the image plane.

To separate the F corona, instrumental stray light, and prior coronal brightness from the CME, we background-subtracted the despiked, noise-gated images using an ad hoc background model constructed from adjacent-in-time images. In particular, we used the pixelwise minimum of the two prior and two subsequent images from each instrument, as an estimate of all background sources. This commonly used technique is particularly useful for isolating bright CMEs from the relatively steady "background corona," as well as from the F corona itself.

One problem we found was that the CME itself displaced pre-existing bright structures (ray-like streamer tops) in the corona. This produced dark artifacts in the CME image, as pre-existing bright streamer tops appeared in the background model. We overcame this difficulty by noting that the streamer tops were nearly radial throughout the COR2 FOV. We transformed the background image to radial coordinates and scaled the radial image by a factor of $r^{2.4}$, where r is the focal-plane radius of each pixel, to approximately remove the radial brightness gradient. With the radial brightness gradient removed, we identified the average normalized brightness of each column, producing a summary number, $NB(\theta)$, where θ is the position angle around the Sun. $NB(\theta)$ indicates the relative brightness of each radial line in the original image compared to other radial lines at other position angles. We then multiplied each column in the non-normalized radialized image by a factor of $\langle NB\rangle/NB(\theta)$ (where the angle brackets denote radial averaging), and finally transformed the data back to image plane coordinates. This produced a background image in which the radial proportional profiles were preserved, but the azimuthal profiles were approximately equalized. The purpose of the normalizing step is to produce a "typical" correction factor for each radius, rather than allowing the correction factor to be dominated by bright pixels at the innermost radius. The process is illustrated in Figure 2. It yielded a smoother background with the correct radial profile and lacking bright radial artifacts "behind" the CME.

We calculated separate background images for the B and pB images of the event, using the same technique for each image type. This produced separate background-subtracted B and pB images that were similarly processed and therefore directly comparable for the purpose of ratio analysis. The background identification and subtraction process, in particular, helps to isolate the CME from the background corona. This is important because each of B and pB are accumulated along an entire line of sight. Isolating the "feature excess" contribution in the particular feature is important for the direct ratio pB/B, which we use below to infer the 3D location, to be meaningful.

The pB/B brightness ratio, in particular, yielded surprising structure that is not immediately apparent in either the B or pB image. Figure 3 shows three views of the 2010 April 3 CME from *STEREO-A*: B (unpolarized), pB (excess tangential polarized), and pB/B (ratio). The pB image clearly emphasizes different aspects of the CME from the B image; but the ratio highlights the 3D structure. It is worth noting that these images are highly smoothed by the noise-gating process; the photometric S/N in any one COR2 pixel is below unity, and the noise-gating has therefore rejected nearly all small scale information from the image. S/N on the represented scales in Figure 3 is ~10–30 (depending on location within the image).

The ratio of pB/B in each bright feature measures the out-of-plane angle ξ of that feature. In the context of eclipse and coronagraphic analysis, the analytically precise polarization formula is quite complex and is usually evaluated using the qvan de Hulst coefficients (e.g., Billings 1966; Howard & Tappin 2009). At higher altitudes above $\sim 2\,R_\odot$, the Sun may be treated as a point source, and the resulting approximate polarization formula is readily invertible (DeForest et al. 2013) to obtain the location of compact features in closed form:

$$\xi = \varepsilon \pm \mathrm{asin}\left(\sqrt{\frac{1 - \mathrm{pB}/B}{1 + \mathrm{pB}/B}}\right), \tag{3}$$

where ε is the elongation angle (the radial apparent distance) of a feature from the Sun, and ξ is the angle between the feature–Sun line and the plane perpendicular to the observer's line of sight. This "naïve" formula is valid for heights above 2–4 $R_\odot$ from the Sun, i.e., throughout the the COR2 FOV.

The naïve location formula (Equation (3)) has been explored in the context of error propagation and wide-field imaging by

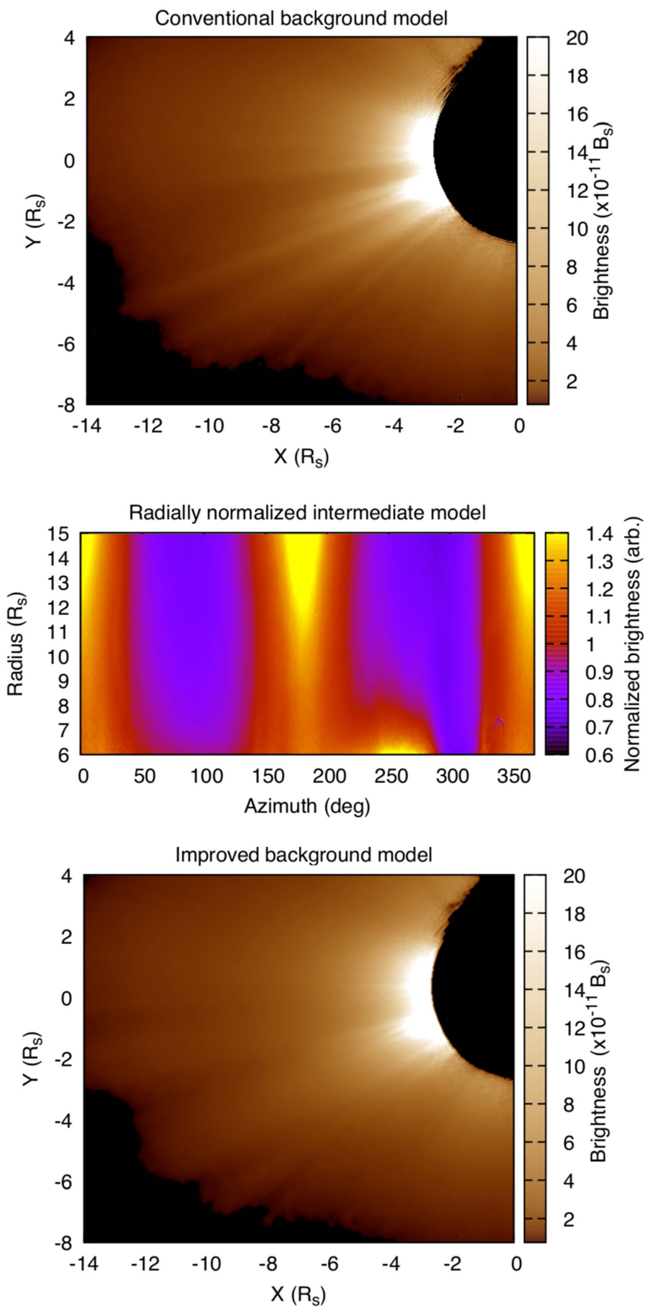

Figure 2. Refinement of the K-coronal background model used for our analysis used azimuthal brightness normalization to remove radial structure. Top: simple background model was assembled from the pixelwise minimum value of the two prior and two subsequent *STEREO*/COR2 images relative to 2010 April 3 11:06. Middle: radial-coordinate normalized-brightness image shows variation from azimuth to azimuth. Bottom: dividing each column of the radial-coordinate image by the normalized brightness average for that column, then transforming it back to instrument coordinates, yields a smoother background model.

DeForest et al. (2013). The $\pm$ in Equation (3) represents the famous front/back ambiguity relative to the Thomson surface. This ambiguity can be overcome by feature tracking in the wide field (in which the feature's radial apparent motion $\Delta\varepsilon$ is non-negligible compared to the right-hand side of Equation (3); e.g., DeForest et al. 2013), or by other means of inference in the narrow field or with a single image (e.g., de Koning & Pizzo 2011). We use stereoscopy, noting (in Figure 1) that the core of the CME and the expected point of tangency between the *SOHO*-observed envelope and the *STEREO-A* line of sight at the *STEREO-A*-observed envelope is near or to the right of the *SOHO*-observed CME centerline. The *SOHO*-observed CME centerline, in turn, is in the near field, as seen from *STEREO-A*.

Placing an observed coronal feature in 3D requires converting between the observer-centric coordinate system, in which features are commonly projected onto a focal plane related to angle from the observer, to a Cartesian one. For the coronagraph FOV and moderate precision ($\sim$0.25 $R_\odot$) in absolute feature placement, it is sufficient to use the orthographic/Cartesian projection and treat features as if they are projected with parallel rays onto the conventional (x,y) coordinates of the focal plane. Then, the z coordinate (by convention, toward the observer) is just

$$z = \tan\xi\sqrt{x^2 + y^2}, \tag{4}$$

where x and y are physical distances in the fictional focal-plane perpendicular to the observer's line of sight and contain the center of the Sun, and z is a physical distance pointing approximately toward the observer.

We used this orthographic projection to place features in the observer-centric x, y, z coordinate system, then used conventional transforms to convert that frame to the natural-for-stereoscopy heliocentric ecliptic coordinate system, which is defined by an origin at the center of the Sun, $+X$ direction directly toward the Earth, and $+Z$ direction directly toward ecliptic north.

4. Results

Figure 4 shows the 3D structure of key features in the CME, which we derived by extracting the out-of-plane angle ξ at each point in the *STEREO-A* image. The *STEREO-A* and *SOHO* focal planes are rendered at the correct angles. The features are rendered in heliocentric ecliptic Cartesian coordinates. The "*STEREO-A* view" reveals the portions of the CME that we located in 3D: two oblique elements of the perimeter and the central bright "C" shape. Only these portions are rendered in 3D in the other panels, to avoid confusion effects in the perspective view.

In the *SOHO* view (left), the central "C" (whose shape is derived from the pB/B ratio shown in Figure 3) corresponds essentially perfectly with a compact, bright feature in the *SOHO*/LASCO image (encircled with a light green, dashed oval in each panel). The feature is also readily visible in the central panel of Figure 1, but the direct altitude comparison does not show it as unambiguously identical to the "C."

Figure 5 contains, in the left panel, a close-up of the "C" in the *STEREO-A* image plane, as seen in standard total brightness, with a parametric curve overlain on the faintly visible "C" itself. The numbers show integrated distance along the curve, in apparent solar radii. The right panel shows the derived out-of-plane distance along the parametric curve.

The error bars in the right panel of Figure 5 are spaced to indicate independent data values after the smoothing that was applied to the data. Their magnitude is calculated based on a posteriori shot noise, using a white noise model and the spatial spectrum of the fully processed data, after noise-gating and subsequent smoothing. Hence, they represent only photometric uncertainty at the focal plane from residual Poisson photon-counting noise, and not uncertainty or error

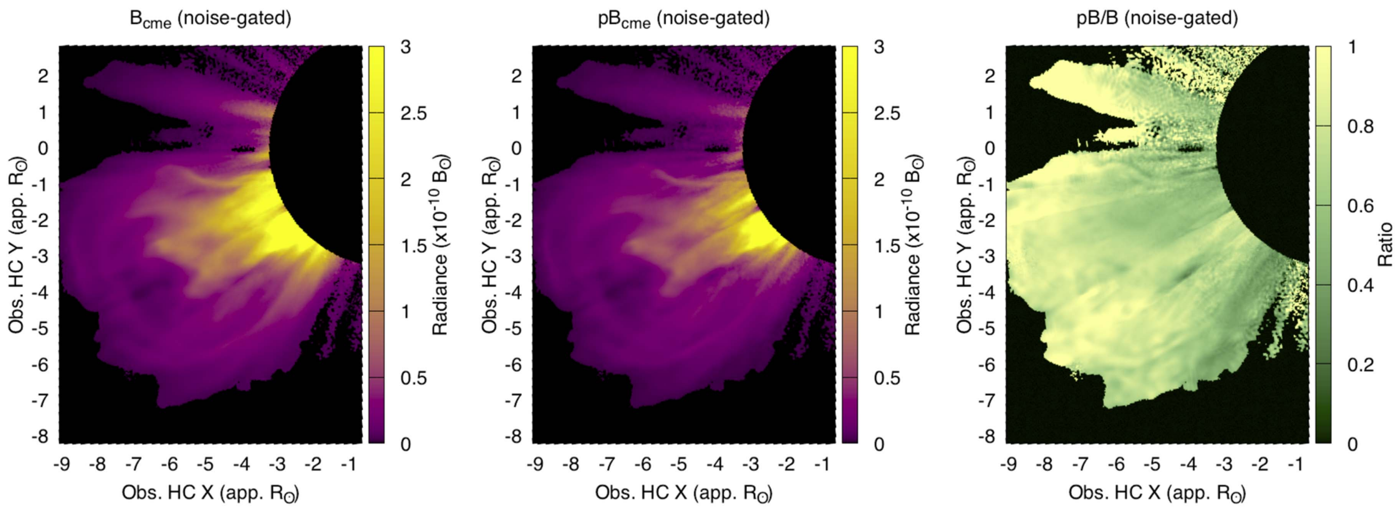

Figure 3. Three noise-gated views of the polarized CME of 2010 April 3, from *STEREO-A*, reveal different aspects of the CME. Left: the B image reveals the broadest cross-section of density structures. Middle: the pB image attenuates out-of-plane features. Right: the pB/B ratio image reveals surprising structure not visible in the B and pB frames. Regions where $B < 2 \times 10^{-11} B_\odot$ are masked and appear black.

introduced by multiple features along the line of sight or by errors in the model background. The error bars are spaced to indicate the approximate distance between independent samples after smoothing.

The small bumps at 0.5 $R_\odot$ and 1.4 $R_\odot$ are within a factor of two of the smoothing length in the final images and may be either photometric noise or residual background artifacts. They are probably not significant compared to residual photometric noise. The overall downward trend in the curve is highly significant and represents actual photometric variation at the focal plane. The general trend shows that the out-of-plane position shifts along the length of the marked curve, from approximately 2.8 ± 0.15 $R_\odot$ out of the plane near the upper portion of the curve to 2.0 ± 0.12 $R_\odot$ out of the plane near the lower part of the curve.

Because the feature is known from the direct stereoscopy (Figure 2) to be in front of the image plane from *STEREO-A*'s perspective, rather than behind it, we identify larger out-of-plane distances as closer to *STEREO-A*. Thus, we conclude that the "C" has a right-handed helical shape, because traversing the near-circular curve in Figure 5 in a clockwise direction causes a displacement into the page. A perfect helix with no measurement noise would yield a smooth diagonal line in the right-hand panel of Figure 4.

This view of the feature as having right-handed chirality is corroborated by the shape of the corresponding feature in the LASCO images. The feature is seen to slant up and rightward in Figures 2 and 4, which agrees with the chiral sense derived from the plot in Figure 5.

The chirality of the CME's density structure is of interest because it presumably traces the shape of the CME's internal magnetic field: the CME structure forms deep in the corona where the plasma β parameter is low and density structures are confined by the field. During propagation, those structures are generally preserved, in part because the entire system can become causally disconnected as it propagates outward (e.g., Owens et al. 2017).

The shift in out-of-plane location seen in the right-hand panel of Figure 4 corresponds to a shift in pB/B ratio in the background-subtracted feature, from approximately 0.76 near the beginning to 0.81 near the end of the identified curve in Figure 5. This represents a differential shift of well under 1% of the raw signal in the Level 0 data.

5. Comparison to in situ Data

The 2010 April event under study has been analyzed by Möstl et al. (2010) and the flank of the CME was found to have hit the *Wind* and *ACE* spacecraft (mission descriptions in Acuña et al. 1995 and Stone et al. 1998). In particular, Möstl et al. traced the path of this particular CME through the *STEREO-A*/HI-1 and HI-2 FOVs. They verified, both from the tracking and from in situ data from the *WIND* spacecraft, that the northern flank of the CME impacted Earth, *ACE*, and *WIND* midway through 2010 April 5.

Möstl et al. discussed at some length the lack of rotating magnetic structure in this CME as measured in situ by *WIND*, and its implications for magnetic cloud identification and flux-rope modeling. We focus on the cloud portion at the beginning of the ICME ejecta, for which we can determine the chirality since there is a clear magnetic cloud rotation and well-understood propagation geometry.

We examined the magnetic data from the magnetometer on board the *ACE* spacecraft (*ACE*/MAG; Smith et al. 1998) and compared it to a cartoon model of a flux rope, to determine whether or not the magnetic chirality agreed with the morphological chirality we found in Section 4.

To illustrate the expected behavior of the magnetic field, Figure 6 shows a cartoon rendering of a generic right-handed flux rope in the familiar Radial, Tangential, Normal (RTN) coordinate system.[3] If the flux rope is considered to be traveling in roughly the $+R$ direction, then an in situ track of the magnetic field at the CME flank taken along the R direction, in the locus marked with a cyan rectangle, will yield approximately constant magnetic field along the short $\pm R$-aligned chord through the flux rope.

[3] Recall: RTN is a locally Cartesian polar coordinate system. R is the radial direction from Sun center to an observer; T is the direction of $\Omega \times R$ (where Ω is the direction of the Sun's spin pseudovector), and N points in the third direction (which is close to solar north, for observers close to the ecliptic plane).

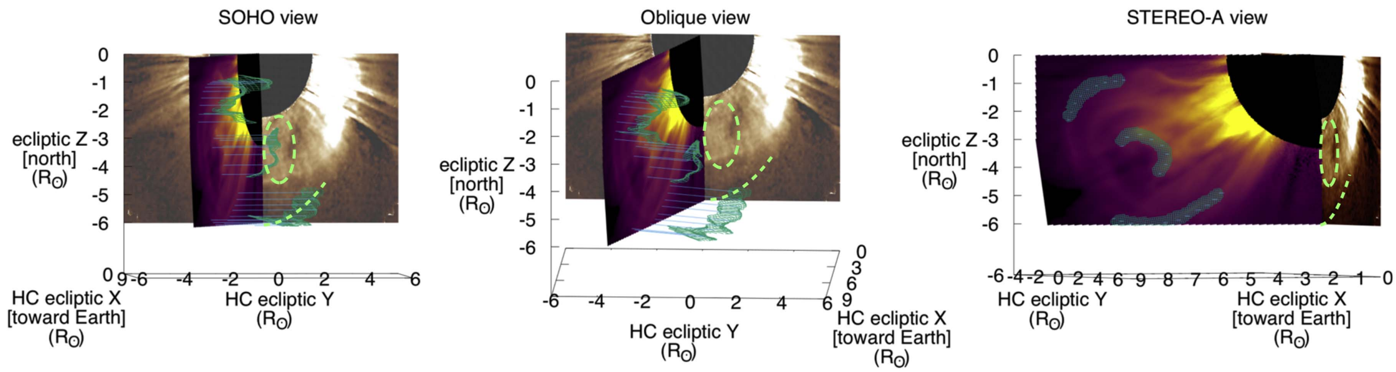

Figure 4. Three different perspective views of the 3D CME of 2010 April 3 11:08 UT show the 3D location of selected features and their position on the *SOHO* and *STEREO-A* focal planes, respectively. The *STEREO* perspective view (right) shows the selected bright edges and the central "knot" of the CME. The oblique view (center) shows the location of the features in 3D. The *SOHO* view (left) reveals that, as expected, the southern bright "edge" of the CME in the *STEREO* view coincides with the compressed material at the boundary of the CME at the locus where the *STEREO* line of sight is tangent to the boundary (the green dashed arc). It also reveals that the compact bright feature corresponds well with the central brightening seen with *SOHO* (the green ellipse).

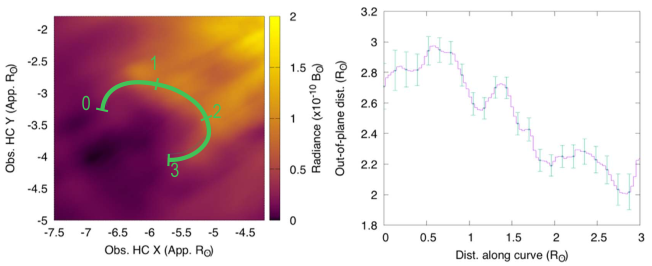

Figure 5. CME core seen in unpolarized light (left) is revealed to be right-hand chiral by 3D inversion of the polarization signal on the indicated line (right). The clockwise end of the curve is 0.7 $R_\odot$ closer to the plane of the sky than the widdershins end. Error bars are derived from the a posteriori statistical properties of the *pB* and *B* images (see the text).

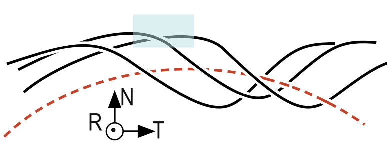

Figure 6. Simple cartoon of a right-handed flux rope shows the relationship between chirality and the nearly fixed field direction in the flank of the flux rope. A curved centerline (the red dotted curve) is surrounded by helical field lines (three are shown). The familiar RTN coordinate axes are shown. The shaded rectangle shows a locus near the flank of the flux rope. See the text for discussion.

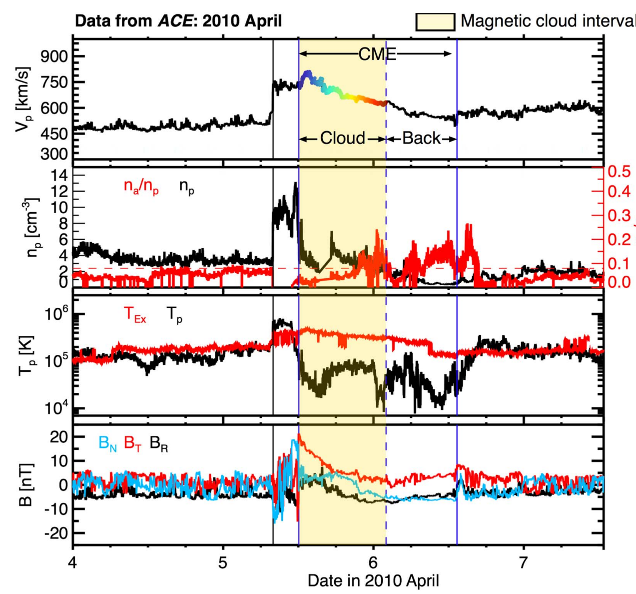

Figure 7. Several solar wind and magnetic field parameters seen by *ACE* show a chordal "cut" through the north flank of the CME shown in Figures 1–4. The yellow interval marks the CME, as identified by Möstl et al. (2010) with *Wind* data, as a cloud with clear magnetic field rotation. Figure 8 shows magnetic field during the CME's passage.

The direction of this near-constant flank magnetic field is determined by the chirality of the flux rope. As should be clear from the figure, a cut through the northern portion of a right-handed flux rope (whose axis is nearly along the T direction) should yield T and R components with the same sign: either $(+T, +R)$ or $(-T, -R)$. A left-handed flux rope should yield opposite signs for the two components: either $(-T, +R)$ or $(+T, -R)$.

We examined the RTN components of the measured magnetic field from *ACE*/MAG, together with solar wind data from *ACE's* Solar Wind Electon Proton Alpha Monitor (*ACE*/SWEPAM; McComas et al. 1998), during the flux-rope crossing associated with this CME. Figure 7 shows wind speed (V_p), density (n_p), alpha-particle abundance (n_a/n_p), temperature (T_p and T_{Ex}), and vector magnetic field (B_R, B_T, B_N) over a 3.5 day interval surrounding the CME encounter, which is marked in yellow. T_{Ex} is the expected temperature of the solar wind using a steady-wind heuristic model, and the T_{Ex}/T_p ratio, in particular, is useful for highlighting CME plasma (Richardson & Cane 1995). The CME interval marked in Figure 7 is the interval identified by Möstl et al. (2010) on the basis of *WIND* data, which agrees moderately well with the *ACE* results. The thermal and magnetic signatures of the CME are clear, though the plasma β parametric signature (not shown) is marginal.

Figure 8 shows the evolution of the magnetic field during the passage of the flux-rope flank. During the interval 2010 April 5 12:00–17:00, the magnetic field pointed in the $(+R, +T, +N)$ direction. The field rotated moderately smoothly to the (R, N) plane over the ~16 hr of the interval identified by Möstl et al., finishing in the $(-R, -N)$ direction.

This behavior does not follow the simple progression expected from the geometry in Figure 4: approximately constant B_T and varying B_R, with B_N smoothly changing sign. This discrepancy can be explained via a slight rotation of the flux rope compared to Figure 4.

From Figures 1–3, it is clear that the flux rope is propagating approximately 40° below the plane of the ecliptic. The

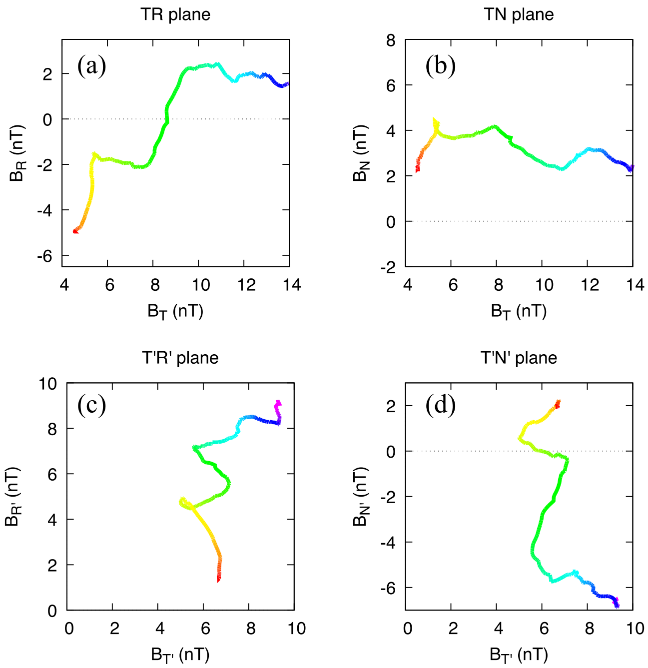

Figure 8. Magnetic evolution plots of (A) the *TR* plane and (B) the *TN* plane reveal the evolution of the magnetic field vector during the CME interval in Figure 7. Time is encoded with color, as in the top panel of Figure 7. Rotating the coordinate system 40° to the right and 40° down reveals tracks in (C) the $T'R'$ plane and (D) the $T'N'$ plane that are consistent with a right-handed helical structure.

flux-rope axis is also not aligned directly transversely. Applying a rotation of 40° about the *N* axis to transform *T* to T' and then a rotation of 40° about T' to yield $R'T'N'$ coordinates yields a better match to the expected field evolution.

Panels (C) and (D) of Figure 8 reveal the magnetic evolution in these modified $R'T'N'$ coordinates and show the expected qualitative behavior of the field. They are also consistent with a glancing chord through the N' side of a right-handed helical flux rope with centerline approximately in the T' direction.

6. Discussion and Conclusions

We have identified the chirality of a bright CME core using the ratio of coronagraphic pB/B from the vantage point of *STEREO-A* and additional large-scale structural clues afforded by simple stereoscopy. This amounts to a differential measurement of the pB/B ratio with precision of the order of a few percent, after background subtraction, in each resolution element (∼4 arcmin) of a smoothed and de-noised coronal image.

Our determination of morphological chirality via polarized imaging is consistent with the inferred chirality of the same structure, as detected in situ by *ACE* during a glancing chordal passage through the CME. The *ACE* determination of right-handed chiral structure provides independent validation of the polarimetric measurement.

Chirality measurement is an important first step toward determining the magnetic field direction in CMEs: chirality relates the strength and direction of the magnetic field in the corona to the observed photospheric field. We verified that the morphological chirality we measured agrees with the magnetic chirality of the same event, determined via in situ sampling, as the CME swept over the *Wind* spacecraft.

Our chirality determination is affected by the famous front/back ambiguity of pB/B measurements; this ambiguity must be resolved in any similar measurement. In the coronagraphic FOV, the Thomson surface is effectively a plane, and the front/back ambiguity requires an external-to-the-instrument measurement (such as stereoscopy). In sufficiently wide-field instruments (FOV wider than ∼30°), the front/back symmetry is broken by the spherical shape of the Thomson surface (e.g., DeForest et al. 2013).

Our out-of-plane measurement of the CME core was noise-limited by the characteristics of the COR2 instrument and its observing program. The photon-counting shot noise in the instrument limits the delicate photometry needed for pB/B ratio determination (and is only partially mitigated by the noise-gating process we applied). Further, the 1 hr cadence, which is limited by the telemetry characteristics of the *STEREO* mission and is also tuned for the primary goal of large-scale CME tracking, prevented a meaningful time-domain analysis of the CME interior features, as they both moved and evolved greatly in the 1 hr interval between each set of polarized triplets. Our measurements were also limited by the crude background model we adopted, which is perfectly adequate for 2D tracking, but is barely adequate for delicate pB/B location work.

Similar determinations of helical structure and other substructure from a future, freshly designed instrument would be improved by greater signal-to-noise ratio in the images and by higher imaging cadence. For example, COR2 operates with a duty cycle of 0.6%. A similar instrument with a shutter duty cycle of 60% would accumulate 100 times more photons, yielding a tenfold improvement in S/N compared to our measurement. Similarly, more rapid observing cadence (enabled by a higher telemetry rate) would permit both improved background models and analysis of structure evolution.

We note that Equation (3) is a compact-feature formula, which directly applies only for features that are small compared to their distance from the Sun. This is the case for small features within CMEs, or even for the region of tangency between a line of sight and a thin shell around a CME, but not for the CME itself. Our demonstration analysis relies on the hypothesis that the CME core was sufficiently compact. As with stereoscopy, truly distributed objects require different techniques that use the polarization images to constrain a geometric model (e.g., Howard et al. 2013).

Our single measurement of 3D substructure within a well-presented CME is a useful demonstration of a hitherto-inaccessible level of precision for the polarization analysis of Thomson-scattered light from CMEs. Such analyses have been limited by the signal-to-noise ratio in existing data sets. This measurement was enabled by a newer post-facto noise-reduction technique (3D noise-gating) that relies on the statistical properties of image noise to separate it from the measurable signal. Future measurements with higher intrinsic signal-to-noise levels will enable more detailed and more common analysis of CME structure than is possible with existing instruments. Such measurements could lead both to better understanding of CMEs and also to a better means of predicting CME geoeffectiveness at Earth (via prediction of B_z direction).

The authors are grateful to the *STEREO* and *ACE* teams for making their data publicly available and to the anonymous referee for good comments that improved the work. This work was funded by the U.S. Air Force, via Projects FA9550-14-1-0296 and FA9550-14-1-0401. *ACE* data analysis was funded by NASA via grant NNX13AQ01G. Image processing was carried out using the Perl Data Language, free software that is available at http://pdl.perl.org.

Facilities: *STEREO*(SECCHI/COR2), *SOHO*(LASCO/C2), *ACE*(SWEPAM, MAG).

Software: Perl Data Language; IDL, SolarSoft.

ORCID iDs

C. E. DeForest https://orcid.org/0000-0002-7164-2786
C. A. de Koning https://orcid.org/0000-0002-9577-1400

References

Acuña, M. H., Ogilvie, K. W., Baker, D. N., et al. 1995, SSRv, 71, 5
Billings, D. E. 1966, A Guide to the Solar Corona (New York: Academic Press)
Brueckner, G. E., Howard, R. A., Koomen, M. J., et al. 1995, SoPh, 162, 357
Crifo, F., Picat, J., & Cailloux, M. 1983, SoPh, 83, 143
Dai, X., Wang, H., Huang, X., Du, Z., & He, H. 2015, ApJ, 801, 39
DeForest, C. E. 2004, ApJL, 617, L89
DeForest, C. E. 2017, ApJ, 838, 155
DeForest, C. E., Howard, T. A., & Tappin, S. J. 2013, ApJ, 765, 44
de Koning, C. A. 2014, in ASP Conf. Ser. 484, Outstanding Problems in Heliophysics: From Coronal Heating to the Edge of the Heliosphere, ed. Q. Hu & G. P. Zank (San Francisco, CA: ASP), 30
de Koning, C. A., & Pizzo, V. J. 2011, SpWea, 9, 03001
Dere, K. P., Wang, D., & Howard, R. 2005, ApJL, 620, L119
Domingo, V., Fleck, B., & Poland, A. I. 1995, SoPh, 162, 1
Howard, R. A., Moses, J. D., Vourlidas, A., et al. 2008, SSRv, 136, 67
Howard, T. A., & Tappin, S. J. 2009, SSRv, 147, 31
Howard, T. A., Tappin, S. J., Odstrcil, D., & DeForest, C. E. 2013, ApJ, 765, 45
Jackson, J. 1962, Classical Electrodynamics (1st ed.; New York: Wiley)
Kaiser, M. L., Kucera, T. A., Davila, J. M., et al. 2008, SSRv, 136, 5
Lyot, B. 1931, LAstr, 45, 248
McComas, D. J., Bame, S. J., Barker, P., et al. 1998, SSRv, 86, 563
Mierla, M., Inhester, B., Antunes, A., et al. 2010, AnGeo, 28, 203
Moran, T. G., & Davila, J. M. 2004, Sci, 305, 66
Moran, T. G., Davila, J. M., & Thompson, W. T. 2010, ApJ, 712, 453
Möstl, C., Temmer, M., Rollett, T., et al. 2010, GeoRL, 37, L24103
Owens, M., Lockwood, M., & Barnard, L. 2017, NatSR, 7
Richardson, I. G., & Cane, H. V. 1995, JGR, 100, 23397
Smith, C. W., L'Heureux, J., Ness, N. F., et al. 1998, SSRv, 86, 613
Stone, E. C., Frandsen, A. M., Mewaldt, R. A., et al. 1998, SSRv, 86, 1
Tousey, R. 1973, in Space Research Conf. 2, ed. M. J. Rycroft & S. K. Runcorn (Paris: ESA), 713